SUPPORTING INFORMATION

Fully solid-state graphene transistors with striking homogeneity and sensitivity for the practicalization of single-device electronic bioassays

Cheng Wang,*[,†,‡] *Jingjing Wu*,[†,§] *Yashuo He*,[†,§] *Ze Song*,[†,‖] *Sumeng Shi*,[†,§] *Yibo Zhu*,[⊥] *Yuan Jia*,*[,#] and *Weixiang Ye**[,▽]

[†]Tianjin Key Laboratory of Wireless Mobile Communications and Power Transmission, [‡]Department of Intelligence Science and Technology, [§]Department of Communication Engineering, and [‖]Department of Electronic Science and Technology, College of Electronic and Communication Engineering, Tianjin Normal University, Tianjin 300387, China

[⊥]Department of Mechanical Engineering, Columbia University, New York 10027, United States

[#]Jiangsu Key Laboratory of Micro-Nano Biomedical Instrument Design and Manufacture, School of Mechanical Engineering, Southeast University, Nanjing 211189, China

[▽]Jiangsu Key Laboratory of Thin Films, School of Physical Science and Technology, Soochow University, Suzhou 215006, China

*Corresponding Authors: cwang@tjnu.edu.cn (C.W.), yjia2218@seu.edu.cn (Y.J.), wxye@suda.edu.cn (W.Y.)

CONTENTS

1 Materials and reagents

4-(2-hydroxyethyl)-1-piperazineethanesulfonic acid (HEPES), 4-mercaptobenzoic acid (MBA), N-hydroxysuccinimide (NHS), N-(3-dimethylaminopropyl)-N′-ethylcarbodiimide hydrochloride (EDC), 1-pyrenebutyric acid N-hydroxysuccinimide ester (PBA-NHS), 3-mercaptopropionic acid N-hydroxysuccinimide ester (MPA-NHS), and 12-mercaptododecanoic acid N-hydroxysuccinimide ester (MDA-NHS), are purchased from Sigma-Aldrich (Shanghai, China). Other chemicals, such as methanol, ethanolamine, $NaNO_3$, HNO_3 are of analytical purity grade.

The DNAzyme sequence 5′–ACA GAC ATC TCT TCT CCG AGC CGG TCG AAA TAG T–3′ and the amino-group modified substrate sequence 5′–NH_2–ACT ATrA GGA AGA GAT GTC TGT–3′ are customized by Sangon Biotech (Shanghai, China).

The HEPES buffer used in this work is prepared by dissolving 50 mM HEPES and 50 mM $NaNO_3$ in ultrapure MilliQ deionized (DI) water. The buffer pH is adjusted to 7.4 via acid-base titration (HNO_3 and NaOH). The ionic strength of HEPES buffers is calculated to be $I \approx 50$ mM.

2 Device fabrication protocol

In this work, the fabrication of both FSS- and SG-GFET devices used the standard ultraviolet photolithography and metal deposition techniques to define device structures. The photolithographic operations used the double-layer lift-off technique (100 nm lift-off resist (LOR) 1A interior layer and 1.3 μm photoresist AZ 601 exterior layer). The atomic layer deposition (ALD) of HfO_2 dielectric layers was achieved through a dry oxidation route using tetrakisethylmethylamidohafnium (TEMAH) precursor $[(CH_3)(C_2H_5)N]_4Hf$ and oxidant O_3. The detailed protocol (**Figure S1**) is given as follows:

1) A *p*-type silicon wafer coated by 100 nm SiO_2 on the surface (boron-doped hole concentration $n_h \approx 2 \times 10^{16}$ cm^{-3}) is used as a substrate (**Figure S1a**). To create the local n^+-type conductive back-gate electrodes complementary to the *p*-type substrate, the photolithographic patterning is carried out. After the patterning development, the implantation of phosphor ions is executed with a beam density of 10^{15} cm^{-2}, and a scanning energy of 150 keV. After a rapid annealing at 1050 °C for 30 s, the local n^+-type back-gate electrodes are created (**Figure S1b**). The depth of back-gate electrodes is approximately 500 nm. The phosphor-doped electron concentration n_e is approximately 10^{18} cm^{-3}.
2) The subsequent steps of photolithographic patterning and BOE etching are carried out to locally remove the 100 nm SiO_2 scattering layer and expose the back-gate electrodes (**Figure S1c**).
3) After a thorough cleaning in oxygen plasma (800 mTorr, 950 mW, 3 min), the wafer is then undergone the ALD growth of 15 nm back-gate HfO_2 dielectric layer (**Figure S1d**). TEMAH and O_3 reacting at 120 °C form an isotropic HfO_2 layer[1-4].
4) The pre-synthesized CVD graphene is transferred overlying back-gate HfO_2 dielectric layer. Then, another photolithographic step is carried out to pattern the graphene sheet into square sensing units (20 μm × 20 μm) overlying corresponding back-gate electrodes (**Figure S1e**). Oxygen plasma etching is used to remove the unwanted graphene.
5) A separate photolithographic patterning and metal deposition process are executed in order to define the drain/source electrodes that are made of Cr/Au (5 nm/45 nm). At this point, the fabrication of SG-GFET devices is completed (**Figure S1f**).
6) Building on the SG-GFET devices, a 10 nm top-layer HfO_2 is grown to complete the encapsulation of graphene sensing units. To avoid the global overlay of HfO_2 on the drain/source electrodes, a photolithographic step is carried out prior to the second ALD growth. After the patterning development and the top-layer HfO_2 lift-off, the drain/source electrodes are exposed for the optional pad deposition or lead frame wire bonding (**Figure S1g**).
7) Finally, the metal floating electrodes made of Cr/Au (5 nm/45 nm) are defined using photolithographic patterning and metal deposition. As shown in **Figure S1h**, the fabrication of FSS-GFET devices is completed.

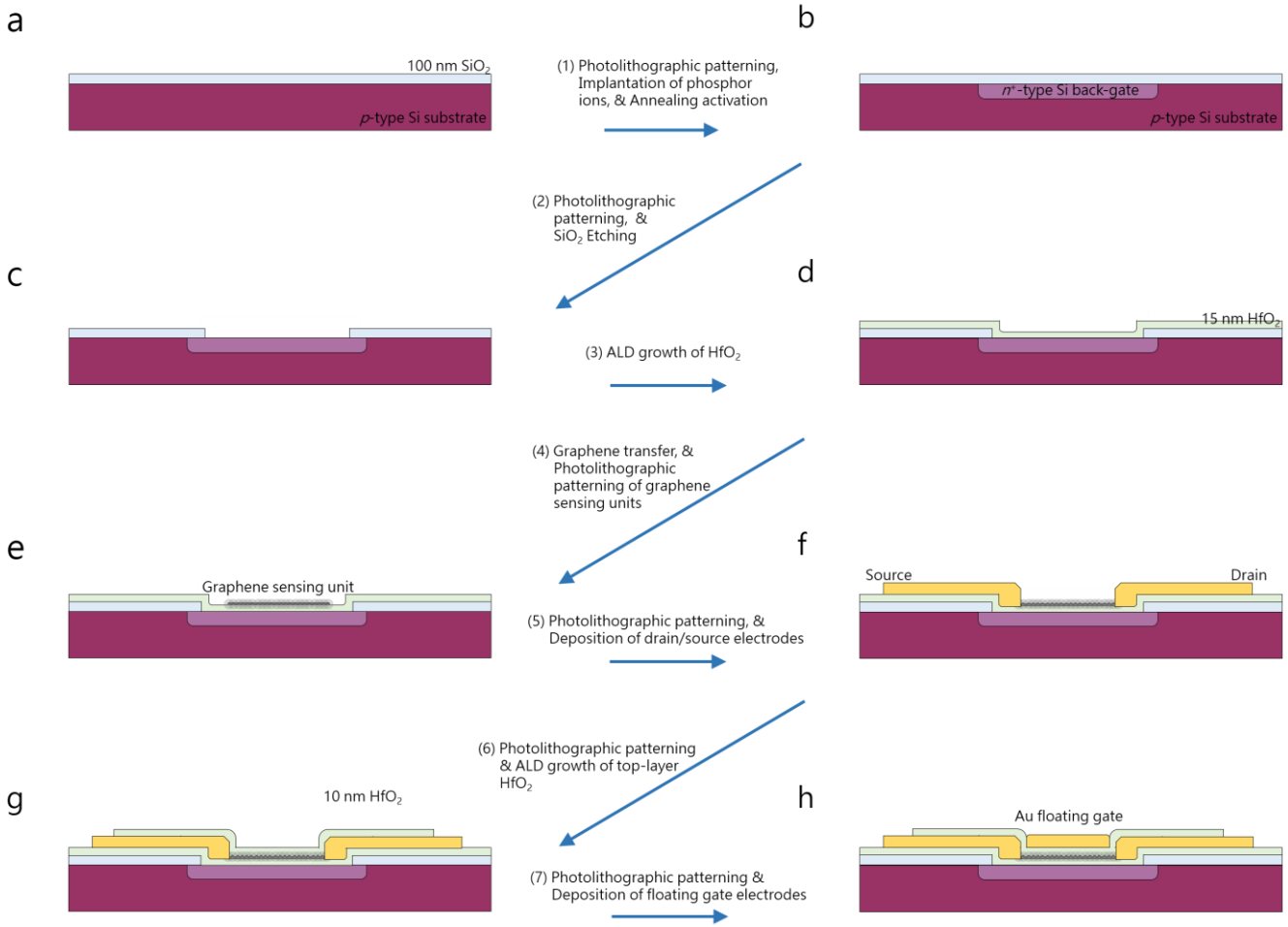

Figure S1. Fabrication protocol of the GFET devices. The 100 nm SiO_2/Si wafer (a) used as the *p*-type substrate is implanted by phosphor ions to create the local complementary n^+-type back-gate electrodes (b). After the removal of SiO_2 scattering layer above the back-gate electrodes (c), a layer of 15 nm HfO_2 is grown by ALD (d). The monolayer CVD graphene sheet is transferred and patterned into graphene sensing units (e). By depositing drain and source electrodes (f), the fabrication of SG-GFET devices are complete. Then, a layer of 10 nm HfO_2 is grown to encapsulate the graphene sensing units (g). After the final deposition of the metal floating gate, FSS-GFET devices (h) are completed.

3 Biochemical functionalization protocol

For the performance comparison and the further DNAzymatic bioassay of Pb^{2+}, the FSS- and SG-GFET devices were functionalized with 4 different molecular linkers, respectively. As shown in **Figure S2**, the linkers MBA-NHS (24 FSS-GFET devices, as shown in **Figure S2a**), PBA-NHS (16 SG-GFET devices, as shown in **Figure S2b**), MPA-NHS (4 FSS-GFET devices, as shown in **Figure S2c**), and MDA-NHS (4 FSS-GFET devices, as shown in **Figure S2d**) were employed in corresponding biochemical functionalization protocols. The step-by-step protocols are listed as follows:

1) **Immobilization of molecular linkers**

   The immobilization of MBA-NHS linker is achieved by first incubating 24 FSS-GFET devices in a MBA solution (200 μM in methanol) for 2 h (step 1 in **Figure S2a**). Then, the devices are incubated in the aqueous solution containing 1 mM EDC and 20 mM NHS for 5 h, to form the MBA-NHS molecules (step 1′ in **Figure S2a**).

   The immobilization of PBA-NHS linker, the MPA-NHS linker, and the MDA-NHS linker is achieved by incubating the corresponding devices in the linker solutions (all 200 μM in methanol) for 2 h, respectively (step 1 in **Figures S2b – S2d**).

2) **Immobilization of oligonucleotide substrate strands**

   After rinsing the devices with methanol and the HEPES buffer (pH 7.4) in order, the immobilization of oligonucleotide substrate strand is achieved by incubating all devices in the substrate strand solution (1 μM in HEPES) for 2 h (step 2 in **Figures S2a – S2d**).

3) **NHS-group blocking**

   After the immobilization of substrate strands, all the devices are incubated in the 100 mM ethanolamine solution (100 mM in DI water) for 1h to deactivate excessive NHS-groups (step 3 in **Figures S2a – S2d**).

4) **DNAzyme hybridization**

   After rinsing with the HEPES buffer (pH 7.4), the hybridization of DNAzyme strands are achieved by incubating all the devices in the DNAzyme solution (1 μM in HEPES) for at least 2 h (step 4 in **Figures S2a – S2d**). The GFET devices are kept in the DNAzyme solution till the biosensing experiments.

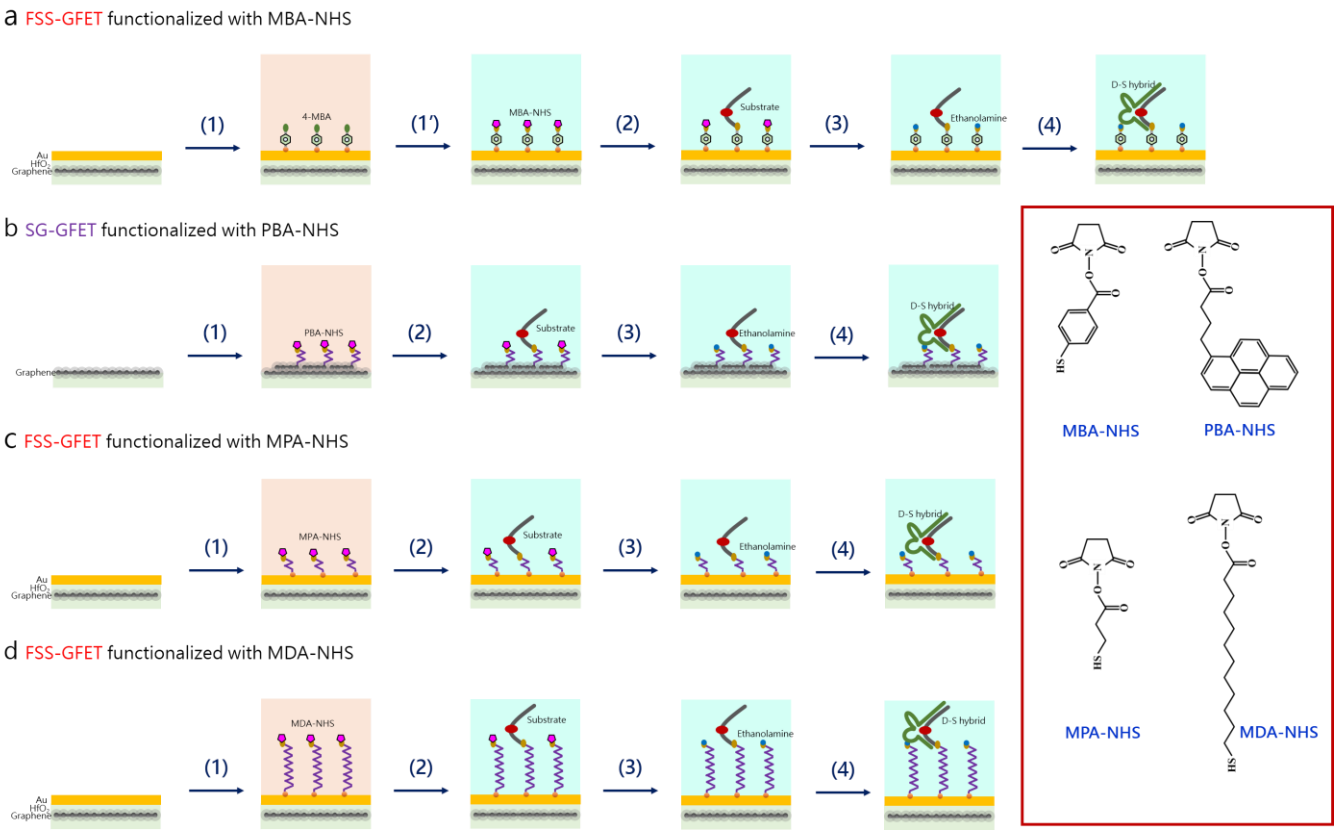

Figure S2. Biochemical functionalization protocols of the GFET devices. 24 FSS-GFET and 16 SG-GFET devices are functionalized with MBA-NHS (a) and PBA-NHS (b) linkers for the device performance comparison. The other 2 nonconductive linkers MPA-NHS (c) and MDA-NHS (d) are used to functionalize 4 FSS-GFET devices, respectively, for the control experiments.

4 Data set of GFET hysteresis characterization

Based on previous investigations, the hysteresis effects inevitably exist in FET devices due to the dielectric layer traps[5] and the interfacial electrochemical transfer (or tunneling) of ambient charges[6]. To understand the hysteresis effects and define suitable conditions for the transfer characteristic curve measurements, we conducted a systematic hysteresis characterization of our FSS- and SG-GFETs in the HEPES buffer (pH ≈ 7.4, ionic strength $I \approx$ 50 mM). Under a constant drain voltage $V_{\mathrm{ds}} =$ 10 mV, the impacts from the gate voltage V_{gs} scanning conditions (forward and backward directions, scanning velocity), and the device states (before functionalization, DNAzyme hybridized, and cleavage completed) were assessed. All the characterization experiments were performed in triplicate using three individual FSS-GFET and SG-GFET devices, respectively. Notably, these devices were disposed after the hysteresis characterization experiments, and not used in further biosensing experiments.

For the FSS-GFETs, three devices were characterized as shown in **Figure S3**. Then the same devices after the DNAzyme functionalization and complete cleavage were again characterized as shown in **Figures S4** and **S5**, respectively. We observed that all devices show little to no effect on hysteresis. Also, under various gate voltage V_{gs} scanning conditions (forward and backward directions, different scanning velocity), the conductivity results are stable and uniform.

For the SG-GFETs, three devices were characterized under the same conditions. The hysteresis characterization results are shown in **Figures S6 – S8**. The SG-GFET devices exhibit the hysteresis dependency with regard to the gate voltage scanning conditions. We attribute this phenomenon to the redistribution and equilibrium of ambient ions in the EDL, which may perform a resonance frequency[6]. At a fast V_{gs} scanning velocity $v =$ 5 V s^{-1}, the forward and backward scanning show significant difference (subfigures (c), (f), (i) in **Figures S6 – S8**). When the scanning velocity is slowed down, the hysteresis becomes weaker (other subfigures in **Figures S6 – S8**).

Consequently, forward scanning with a relatively slow velocity $v =$ 1 V s^{-1} was chosen for the performance comparison experiments to minimize the impacts of hysteresis in SG-GFETs. The conductivity values of SG-GFET devices measured at different fixed voltages are highly comparable to the results obtained from the corresponding transfer characteristic curves (see subfigures (j) in **Figures S6 – S8**). For the FSS-GFETs, the scanning condition is not strictly required. Thus, forward scanning with the velocity $v =$ 1 V s^{-1} was consistently used in this work.

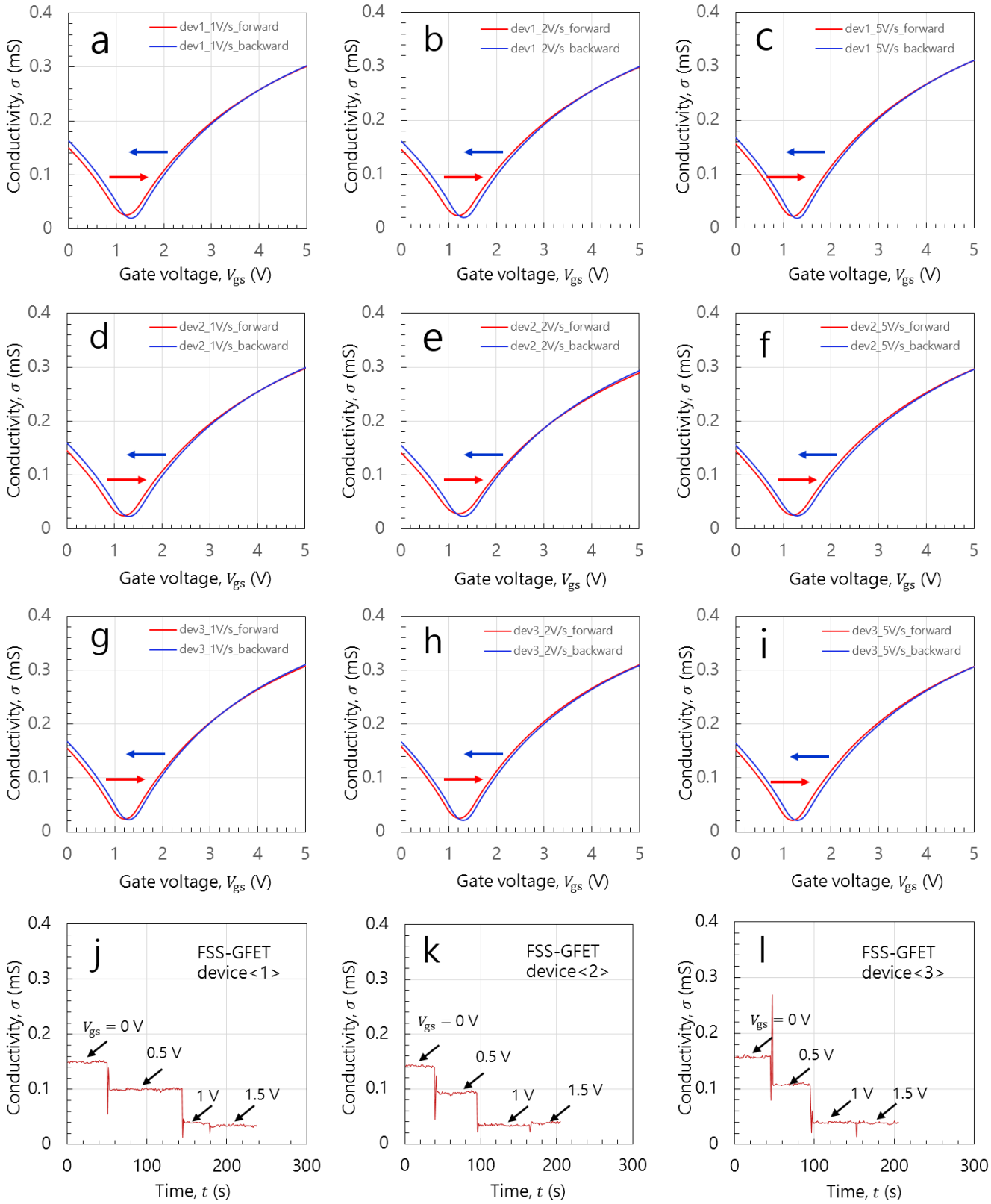

Figure S3. Hysteresis characterization of 3 individual FSS-GFET devices without biochemical functionalization. (a) – (c) Transfer characteristic curves of device <1> measured by scanning gate voltage with the velocity 1 V s^{-1}, 2 V s^{-1}, and 5 V s^{-1}, respectively. (d) – (f) Transfer characteristic curves of device <2> measured by scanning gate voltage with the velocity 1 V s^{-1}, 2 V s^{-1}, and 5 V s^{-1}, respectively. (g) – (i) Transfer characteristic curves of device <3> measured by scanning gate voltage with the velocity 1 V s^{-1}, 2 V s^{-1}, and 5 V s^{-1}, respectively. In (a) – (i), the forward and backward scanning curves are colored by red and blue, respectively. (j) – (l) Conductivity responses of 3 devices measured at the fixed gate voltages of 0 V, 0.5 V, 1 V, and 1.5 V, respectively.

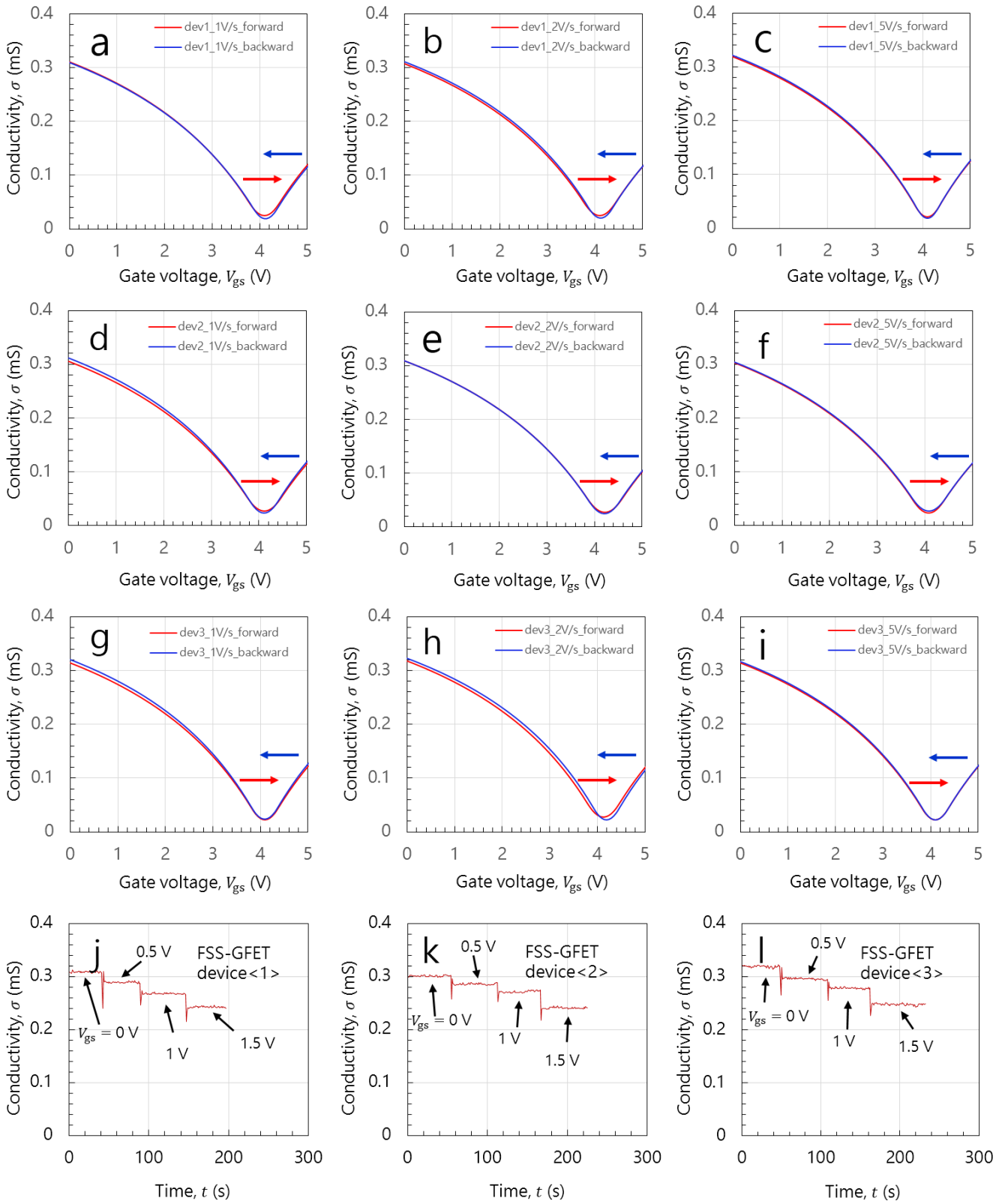

Figure S4. Hysteresis characterization of 3 FSS-GFET devices (same devices in **Figure S3**) with the DNAzyme hybridization functionalization. (a) – (c) Transfer characteristic curves of device <1> measured by scanning gate voltage with the velocity 1 V s^{-1}, 2 V s^{-1}, and 5 V s^{-1}, respectively. (d) – (f) Transfer characteristic curves of device <2> measured by scanning gate voltage with the velocity 1 V s^{-1}, 2 V s^{-1}, and 5 V s^{-1}, respectively. (g) – (i) Transfer characteristic curves of device <3> measured by scanning gate voltage with the velocity 1 V s^{-1}, 2 V s^{-1}, and 5 V s^{-1}, respectively. In (a) – (i), the forward and backward scanning curves are colored by red and blue, respectively. (j) – (l) Conductivity responses of 3 devices measured at the fixed gate voltages of 0 V, 0.5 V, 1 V, and 1.5 V, respectively.

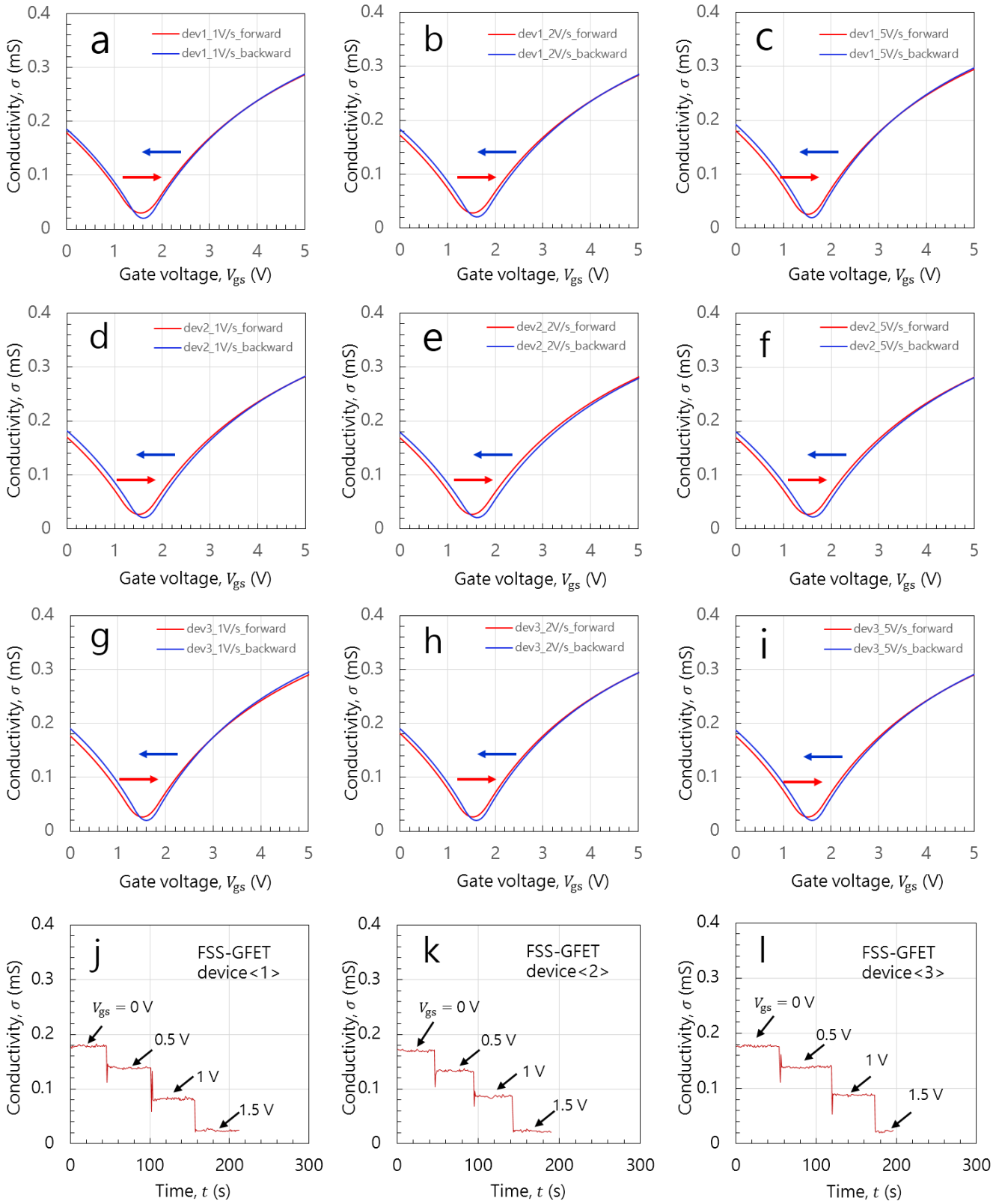

Figure S5. Hysteresis characterization of 3 FSS-GFET devices (same devices in **Figure S3**) after the DNAzymatic cleavage. (a) – (c) Transfer characteristic curves of device <1> measured by scanning gate voltage with the velocity 1 V s^{-1}, 2 V s^{-1}, and 5 V s^{-1}, respectively. (d) – (f) Transfer characteristic curves of device <2> measured by scanning gate voltage with the velocity 1 V s^{-1}, 2 V s^{-1}, and 5 V s^{-1}, respectively. (g) – (i) Transfer characteristic curves of device <3> measured by scanning gate voltage with the velocity 1 V s^{-1}, 2 V s^{-1}, and 5 V s^{-1}, respectively. In (a) – (i), the forward and backward scanning curves are colored by red and blue, respectively. (j) – (l) Conductivity responses of 3 devices measured at the fixed gate voltages of 0 V, 0.5 V, 1 V, and 1.5 V, respectively.

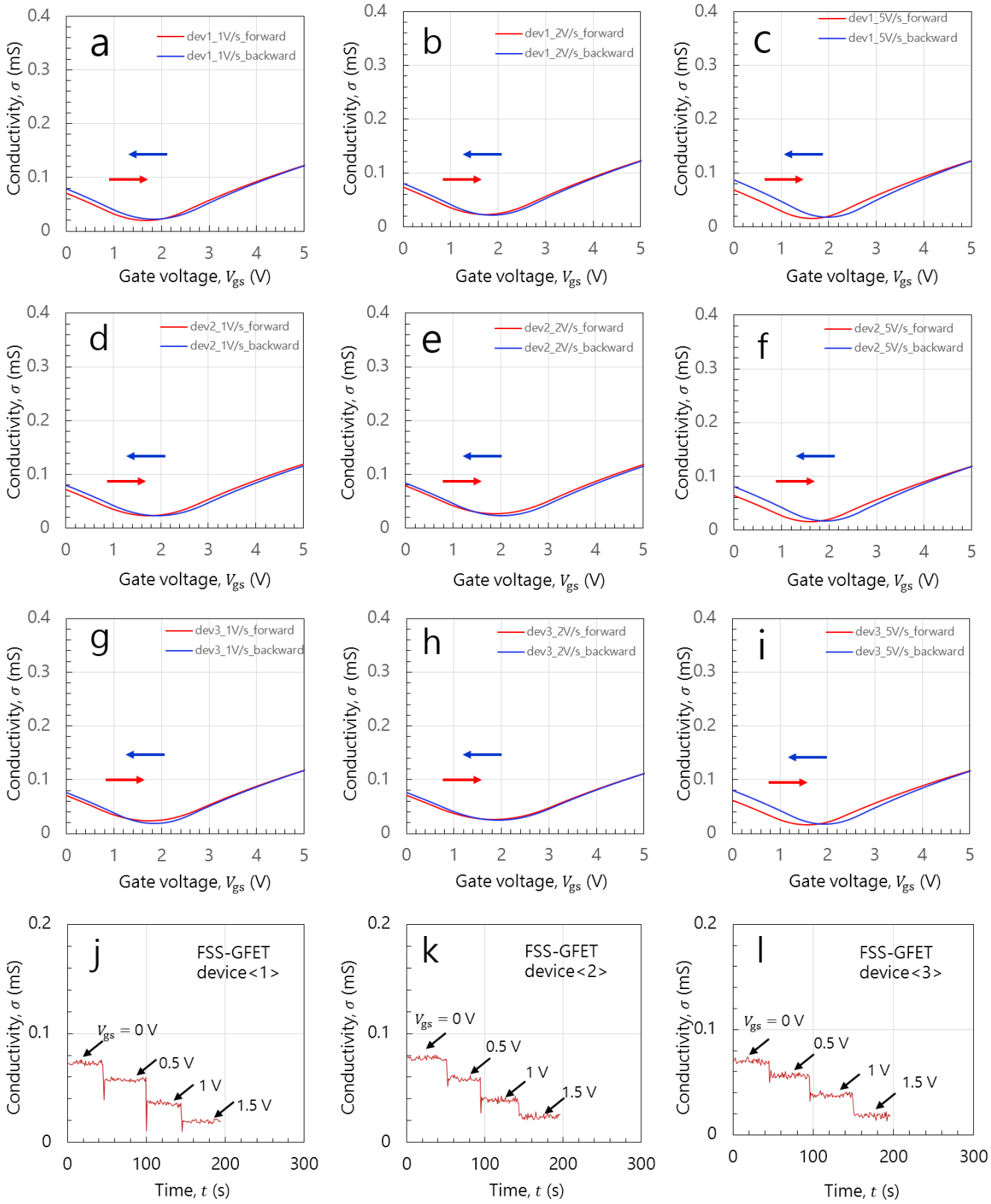

Figure S6. Hysteresis characterization of 3 individual SG-GFET devices without biochemical functionalization. (a) – (c) Transfer characteristic curves of device <1> measured by scanning gate voltage with the velocity 1 V s^{-1}, 2 V s^{-1}, and 5 V s^{-1}, respectively. (d) – (f) Transfer characteristic curves of device <2> measured by scanning gate voltage with the velocity 1 V s^{-1}, 2 V s^{-1}, and 5 V s^{-1}, respectively. (g) – (i) Transfer characteristic curves of device <3> measured by scanning gate voltage with the velocity 1 V s^{-1}, 2 V s^{-1}, and 5 V s^{-1}, respectively. In (a) – (i), the forward and backward scanning curves are colored by red and blue, respectively. (j) – (l) Conductivity responses of 3 devices measured at the fixed gate voltages of 0 V, 0.5 V, 1 V, and 1.5 V, respectively.

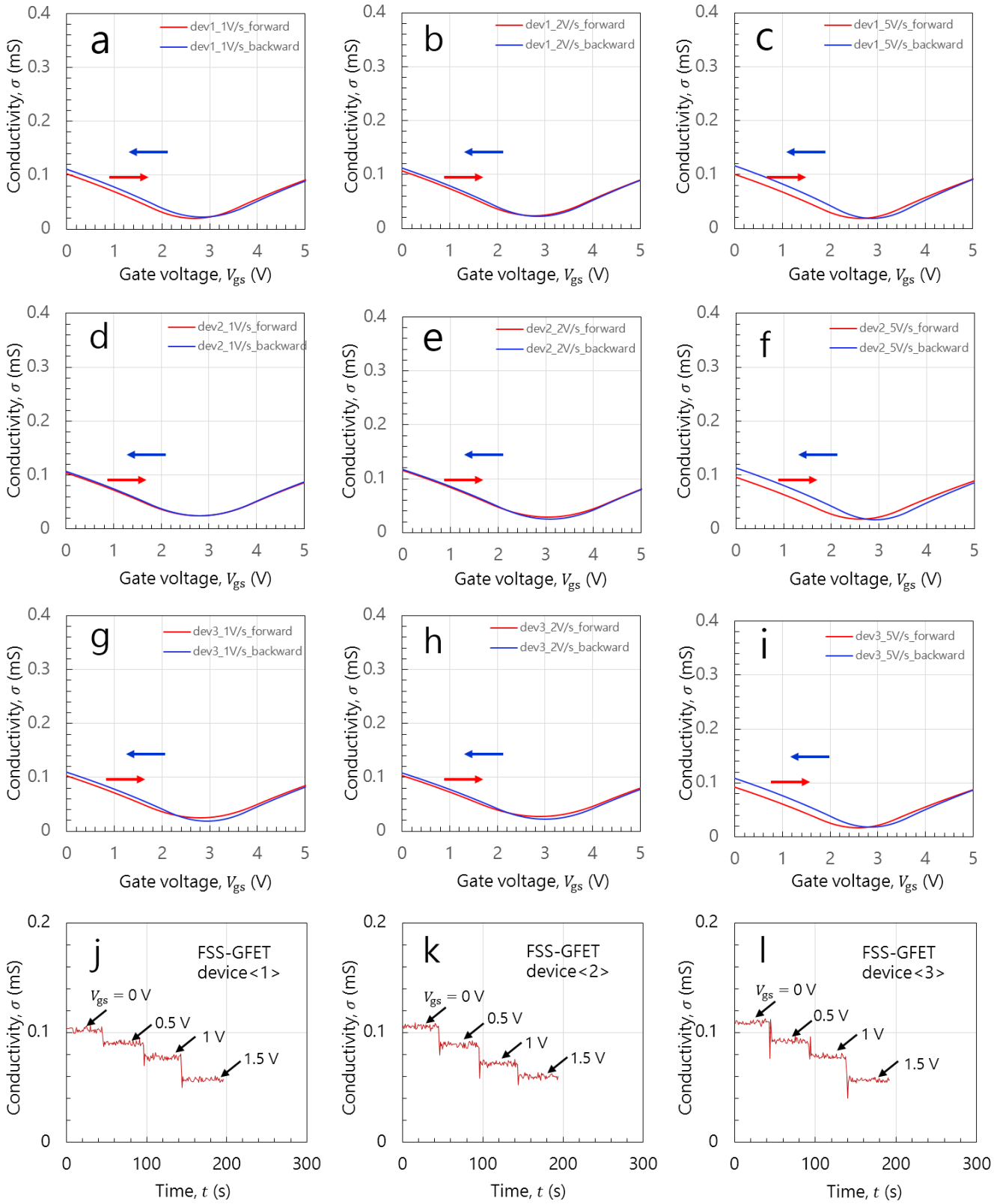

Figure S7. Hysteresis characterization of 3 SG-GFET devices (same devices in **Figure S6**) with the DNAzyme hybridization functionalization. (a) – (c) Transfer characteristic curves of device <1> measured by scanning gate voltage with the velocity 1 V s^{-1}, 2 V s^{-1}, and 5 V s^{-1}, respectively. (d) – (f) Transfer characteristic curves of device <2> measured by scanning gate voltage with the velocity 1 V s^{-1}, 2 V s^{-1}, and 5 V s^{-1}, respectively. (g) – (i) Transfer characteristic curves of device <3> measured by scanning gate voltage with the velocity 1 V s^{-1}, 2 V s^{-1}, and 5 V s^{-1}, respectively. In (a) – (i), the forward and backward scanning curves are colored by red and blue, respectively. (j) – (l) Conductivity responses of 3 devices measured at the fixed gate voltages of 0 V, 0.5 V, 1 V, and 1.5 V, respectively.

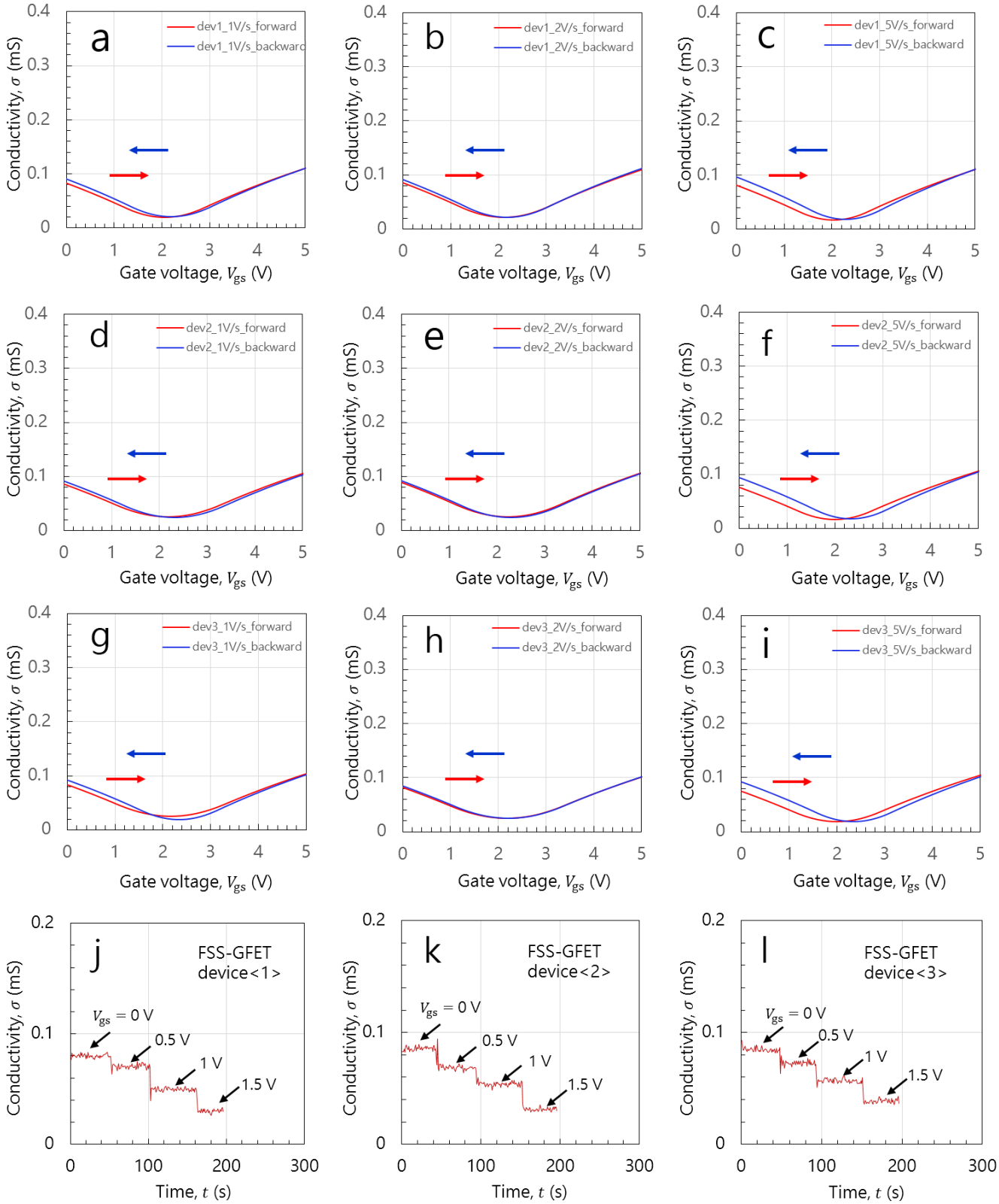

Figure S8. Hysteresis characterization of 3 SG-GFET devices (same devices in **Figure S6**) after the DNAzymatic cleavage. (a) – (c) Transfer characteristic curves of device <1> measured by scanning gate voltage with the velocity 1 V s^{-1}, 2 V s^{-1}, and 5 V s^{-1}, respectively. (d) – (f) Transfer characteristic curves of device <2> measured by scanning gate voltage with the velocity 1 V s^{-1}, 2 V s^{-1}, and 5 V s^{-1}, respectively. (g) – (i) Transfer characteristic curves of device <3> measured by scanning gate voltage with the velocity 1 V s^{-1}, 2 V s^{-1}, and 5 V s^{-1}, respectively. In (a) – (i), the forward and backward scanning curves are colored by red and blue, respectively. (j) – (l) Conductivity responses of 3 devices measured at the fixed gate voltages of 0 V, 0.5 V, 1 V, and 1.5 V, respectively.

5 Data set of GFET transfer characteristics

Here, we present the complete transfer characteristic curves of 32 FSS-GFET devices (24 devices functionalized with MBA-NHS, 4 with MPA-NHS, 4 with MDA-NHS), and 16 SG-GFET devices (all functionalized with PBA-NHS). As shown in **Figures S9 – S12**, for each device, 3 transfer characteristic curves are presented to illustrate the electric properties of the GFETs before functionalization (blue curves), after DNAzyme functionalization (green curves), and after catalytic cleavage (red curves). In particular, the red curves were measured after the kinetic Pb^{2+} biosensing experiments (details included in SI section 6), which included a thorough RNA-cleavage step using the solution of 1 μM Pb^{2+}.

Based on **Figures S9 – S12**, we learned that the FSS-GFETs show better device-to-device performance homogeneity than the SG-GFETs owing to the complete encapsulation of the graphene sensing unit. The blue curves from **Figures S9 – S12**, corresponding to the devices before functionalization, are grouped and compared in the main text **Figures 1d** and **1e**, as a proof of the enhancement of device-to-device homogeneity.

In addition to the device-to-device homogeneity improvement in the transfer characteristics, the FSS-GFETs (**Figure S9**) also homogeneously enhance the transconductance (slope of transfer characteristic curve), and enlarge the lateral shifts with respect to biomolecular interactions. To support the discussion of the two advantages, **Figures S9a** and **S10a** (subfigures with red font titles) are selected as the representatives and presented in the main text **Figures 3a** and **3b**. According to the discussion in the main text, the curve slope enhancement of FSS-GFETs is explained by the graphene mobility protection of the FSS configuration. The larger lateral shifts are attributed to the FSS configuration functionalized by the conductive MBA-NHS linker, which enables a higher gating efficiency by reducing the Debye screening of bioelectronic charges in buffer solutions. As demonstrated in **Figures S11** and **S12**, the FSS-GFET devices functionalized by nonconductive MPA-NHS and MDA-NHS linkers do not show similar levels in the lateral shift of transfer characteristic curves due to the severe Debye screening effect, although the curve slope enhancement remains the same.

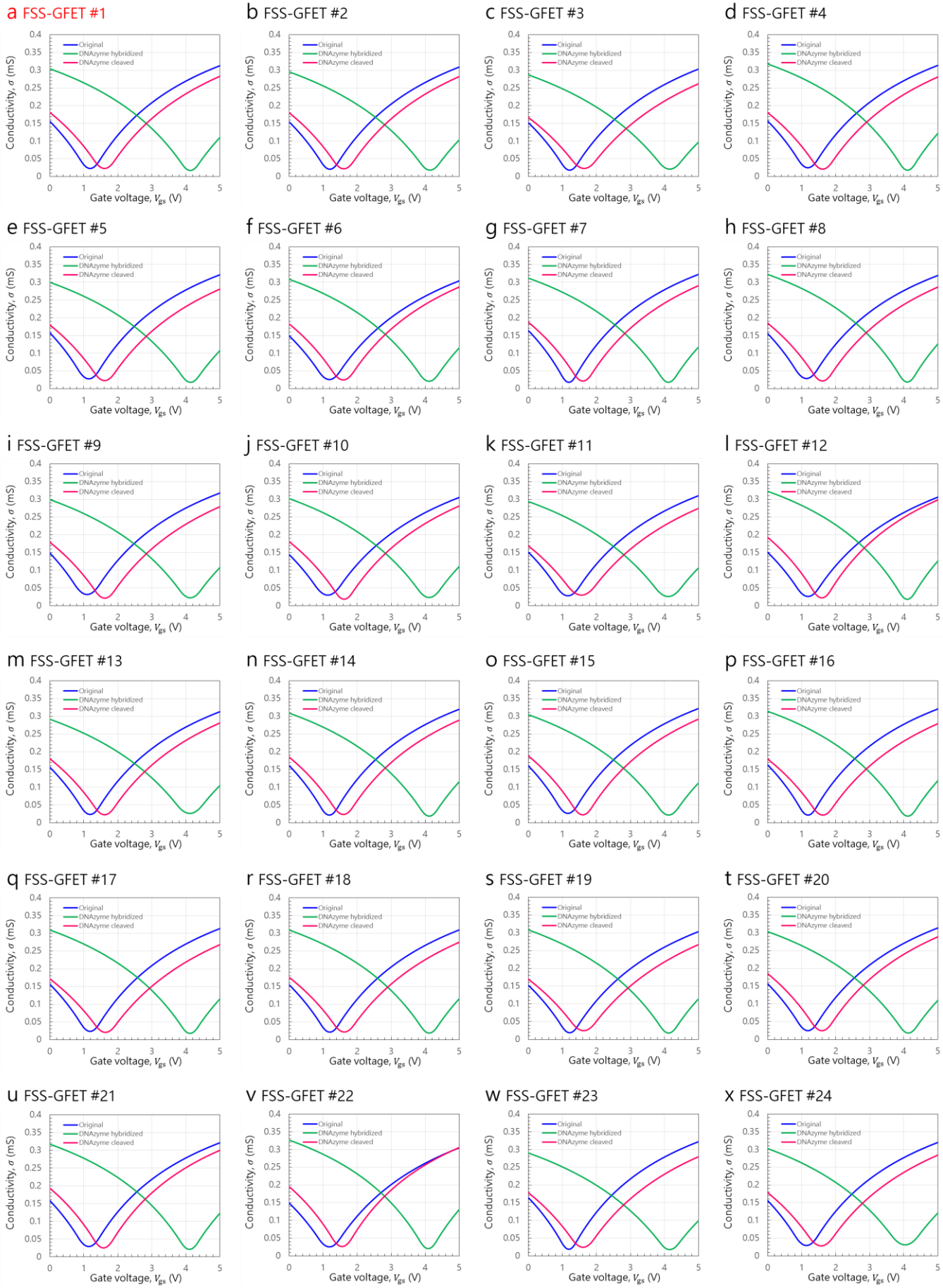

Figure S9. Transfer characteristic curves of 24 FSS-GFET devices using the conductive MBA-NHS linker. All the curves in (a) – (x) perform high homogeneity.

Figure S10. Transfer characteristic curves of the 16 SG-GFET devices using the conventional PBA-NHS linker (nonconductive). The homogeneity and slope of the transfer characteristic curves in (a) – (p) are lower than those of the FSS-GFET devices. In addition, the smaller lateral shift amplitudes with respect to the biomolecular interactions illustrate that the gating efficiency of SG-GFETs is lower than that of FSS-GFETs.

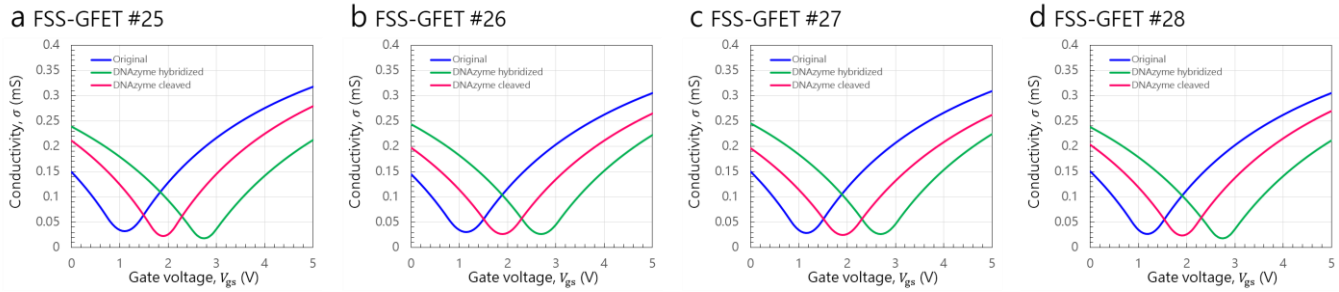

Figure S11. Transfer characteristic curves of the 4 FSS-GFET devices using the nonconductive MPA-NHS linker. In (a) – (d), the advantages of FSS configuration in curve homogeneity and slope are preserved. However, without the conductive linker functionalization to enable the gating efficiency improvement, the lateral shift amplitudes are similar to those of the SG-GFETs as shown in **Figure S10**.

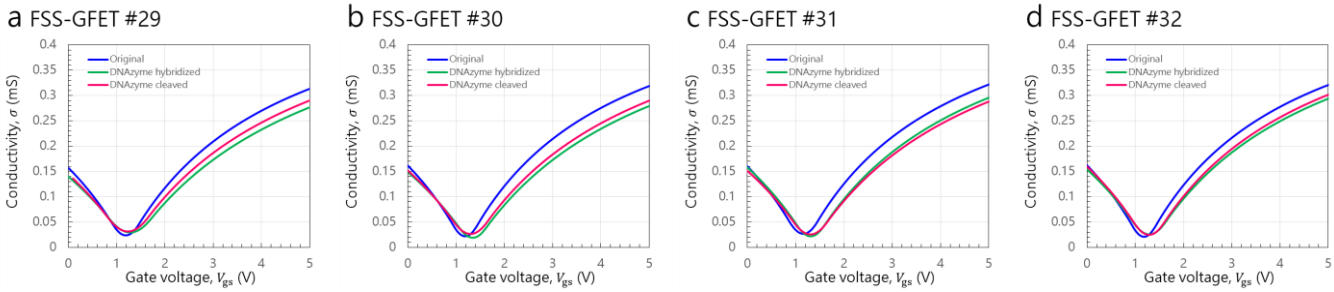

Figure S12. Transfer characteristic curves of the 4 FSS-GFET devices functionalized by nonconductive MDA-NHS linker. In (a) – (d), the advantages of FSS configuration in curve homogeneity and slope are similarly preserved. However, due to the much longer linker size, a more severe Debye screening effect leads to the lateral shifts almost indistinguishable.

6 Data set of biosensing kinetics

The Pb^{2+} samples at various concentrations were prepared using the HEPES buffer (pH ≈ 7.4, I ≈ 50 mM) and detected by the FSS- and SG-GFET biosensors, respectively, via the kinetic observation of time-resolved conductivity responses. In each experiment, the DNAzyme-incubated device was first rinsed by the HEPES buffer for 15 min with a microfluidic system. Then, the Pb^{2+} sample was introduced for a 30-min measurement period. After that, the 1 μM Pb^{2+} solution was introduced to finish the catalytic cleavage.

The complete experimental results of 24 FSS-GFET biosensors and 16 SG-GFET biosensors are presented in **Figures S13** and **S14**. Clearly, the FSS-GFET results show a significantly larger dynamic range. As a result, under a certain noise level of amperometer, the FSS-GFETs possess a much higher sensing capability than that of SG-GFETs. In **Figures S13** and **S14**, the subfigures with red font titles are selected as the representatives and presented in the main text **Figure 4**.

The conductivity responses of each device that are observed at t = 180 s and t = 900 s are extracted from **Figures S13** and **S14**, and fitted by linear functions (see detailed statistical results in **Tables S1** and **S2**). For the FSS-GFETs as shown in **Figure S13**, the calibration curves of 180 s- and 900-s responses are fitted as $R_{\mathrm{FSS}}^{180}(c) = \Delta\sigma_{\mathrm{FSS}}^{180}(c) = -2.935 \times 10^{-4} - 3.633 \times 10^{-3}$, and $R_{\mathrm{FSS}}^{900}(c) = \Delta\sigma_{\mathrm{FSS}}^{900}(c) = -1.940 \times 10^{-3} - 2.567 \times 10^{-3}$, respectively. Hence, the sensitivity parameters are S_{FSS}^{180} = –2.935 × 10^{-4} mS pM^{-1}, and S_{FSS}^{900} = –1.940 × 10^{-3} mS pM^{-1}. The standard deviations are calculated as $\chi_{\mathrm{FSS}}^{180}$ = 6.080 × 10^{-3} mS, and $\chi_{\mathrm{FSS}}^{900}$ = 6.012 × 10^{-4} mS. The LOD performances are estimated as $\mathrm{LOD}_{\mathrm{FSS}}^{180} = 3\left|\chi_{\mathrm{FSS}}^{180}/S_{\mathrm{FSS}}^{180}\right| \approx$ 62.148 pM, and $\mathrm{LOD}_{\mathrm{FSS}}^{900} = 3\left|\chi_{\mathrm{FSS}}^{900}/S_{\mathrm{FSS}}^{900}\right| \approx$ 929.8 fM. The subpicomolar LOD almost approaches the confidence limit of the Pb^{2+} detection in aqueous-media, because the MilliQ DI water solvent also contributes approximately 100 – 200 fM background concentration of Pb^{2+} based on our ICP-MS analysis results (XSeries II ICP-MS, Thermo-Fisher Scientific).

In comparison, for the SG-GFETs as shown in **Figure S14**, the calibration curves of 180-s and 900-s responses are fitted as $R_{\mathrm{SG}}^{180}(c) = \Delta\sigma_{\mathrm{SG}}^{180}(c) = -4.526 \times 10^{-5} - 1.203 \times 10^{-3}$, and $R_{\mathrm{SG}}^{900}(c) = \Delta\sigma_{\mathrm{SG}}^{900}(c) = -3.396 \times 10^{-4} - 1.284 \times 10^{-3}$, respectively. Hence, the sensitivity parameters are S_{SG}^{180} = –4.526 × 10^{-5} mS pM^{-1}, and S_{SG}^{900} = –3.396 × 10^{-4} mS pM^{-1}. The standard deviations are calculated as χ_{SG}^{180} = 3.581 × 10^{-3} mS, and χ_{SG}^{900} = 2.413 × 10^{-3} mS. The LOD performances are estimated as $\mathrm{LOD}_{\mathrm{SG}}^{180} = 3\left|\chi_{\mathrm{SG}}^{180}/S_{\mathrm{SG}}^{180}\right| \approx$ 237.341 pM, and $\mathrm{LOD}_{\mathrm{SG}}^{900} = 3\left|\chi_{\mathrm{SG}}^{900}/S_{\mathrm{SG}}^{900}\right| \approx$ 21.320 pM.

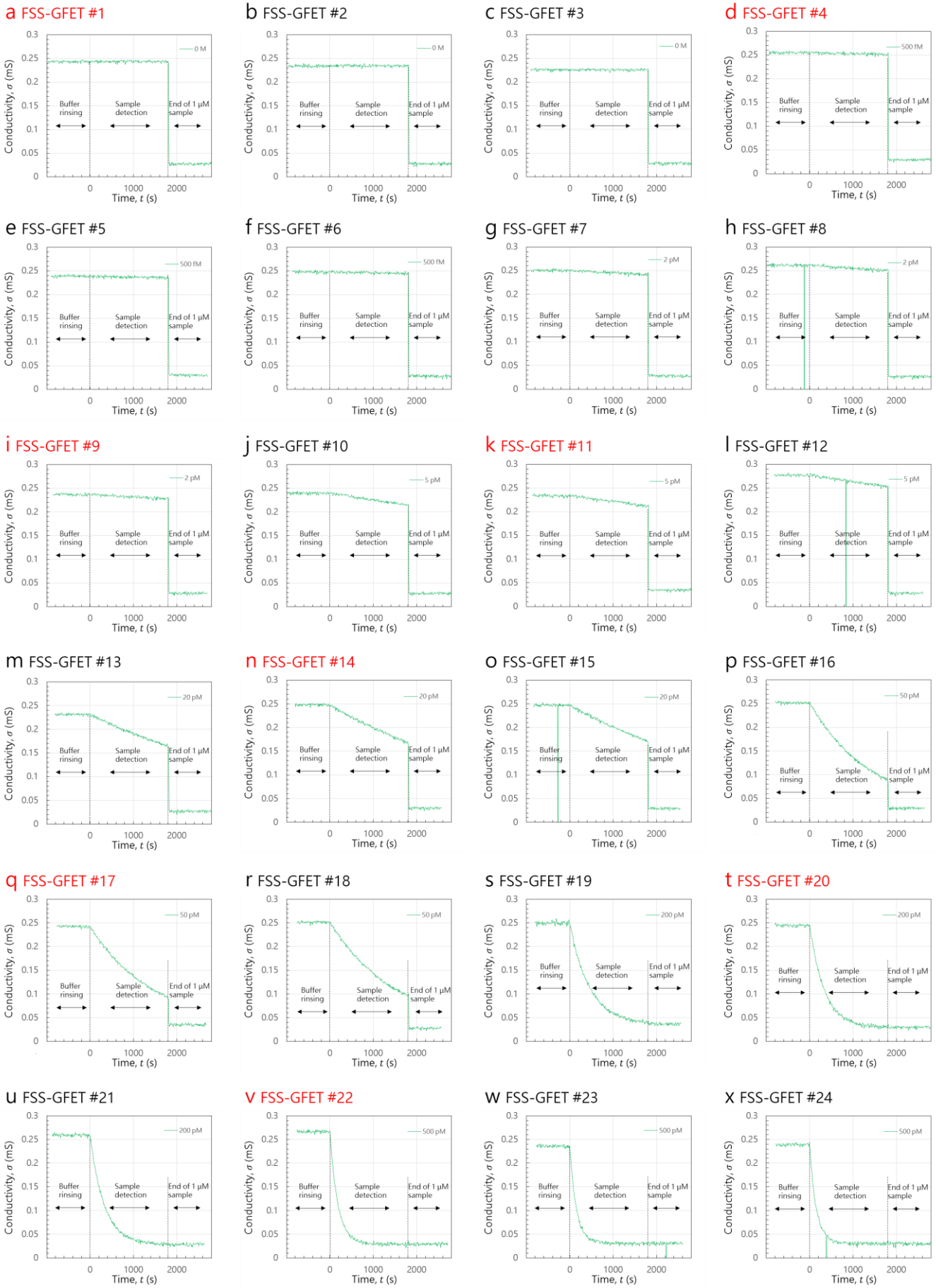

Figure S13. Kinetic processes of the DNAzymatic analysis of Pb^{2+} using 24 FSS-GFET biosensors.

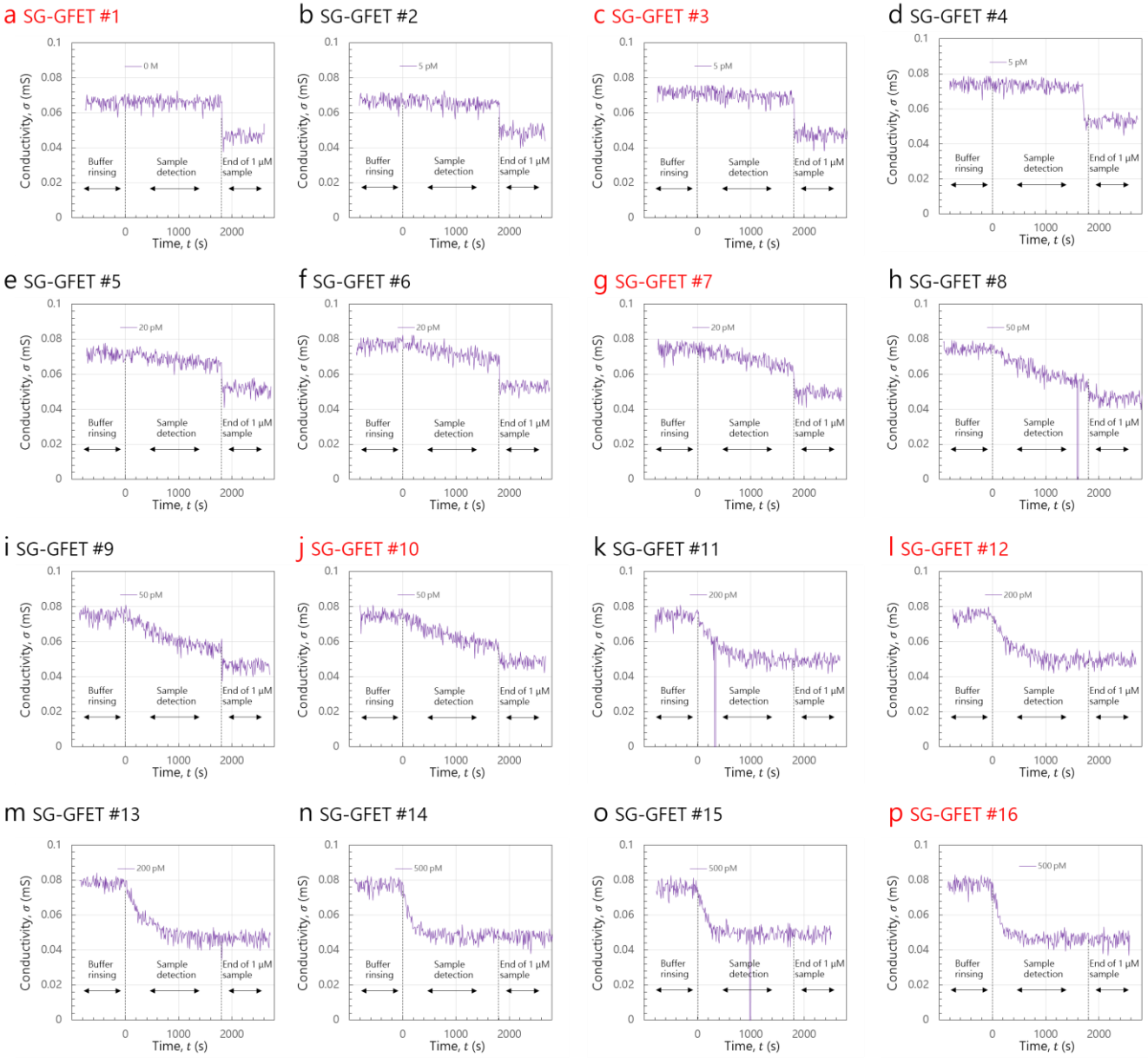

Figure S14. Kinetic processes of the DNAzymatic analysis of Pb^{2+} using 16 SG-GFET biosensors.

Table S1. Statistical results of Pb^{2+} detection results from FSS-GFETs.

Pb^{2+} Conc. c (pM)	**Device number (i)**	**180-s observation**		**900-s observation**	
		Conductivity variation $R_{FSS}^{180}(c) = \Delta\sigma_{FSS}^{180}(c)$ (mS)	**Linear calibration value $\hat{R}_{FSS}^{180}(c)$ (mS)**	**Conductivity variation $R_{FSS}^{900}(c) = \Delta\sigma_{FSS}^{900}(c)$ (mS)**	**Linear calibration value $\hat{R}_{FSS}^{900}(c)$ (mS)**
0	FSS-GFET#1	-0.003842268	-0.00352117	-0.002242268	-0.002533711
	FSS-GFET#2	0.002025773		-0.002374227	
	FSS-GFET#3	0.000553333		-0.002346667	
0.5	FSS-GFET#4	-0.001046809	-0.003668079	-0.003846809	-0.00350444
	FSS-GFET#5	0.000568889		-0.003231111	
	FSS-GFET#6	-0.003083908		-0.003083908	
2	FSS-GFET#7	-0.001535556	-0.004108805	-0.005535556	-0.00641663
	FSS-GFET#8	-0.001345455		-0.006145455	
	FSS-GFET#9	-0.000904651		-0.006204651	
5	FSS-GFET#10	-0.002284536	-0.004990258	-0.012084536	-0.012241009
	FSS-GFET#11	-0.001224138		-0.012424138	
	FSS-GFET#12	-0.000934146		-0.012334146	
20	FSS-GFET#13	-0.005697531	-0.009397521	-0.041297531	-0.041362902
	FSS-GFET#14	-0.00943		-0.04263	
	FSS-GFET#15	-0.00949759		-0.04249759	
50	FSS-GFET#16	-0.027092405	-0.018212046	-0.100192405	-0.09960669
	FSS-GFET#17	-0.025484416		-0.099084416	
	FSS-GFET#18	-0.024440789		-0.098540789	
200	FSS-GFET#19	-0.07098875	-0.062284675	-0.19688875	N/A
	FSS-GFET#20	-0.07395125		-0.20045125	
	FSS-GFET#21	-0.07682069		-0.21052069	
500	FSS-GFET#22	-0.149061842	-0.150429932	-0.228461842	N/A
	FSS-GFET#23	-0.142880263		-0.202080263	
	FSS-GFET#24	-0.143438462		-0.210438462	
Standard deviation (mS)		$\chi_{FSS}^{180} = \sqrt{\frac{1}{24-1}\sum_{i=1}^{24}\left(R_{FSS\_i}^{180} - \hat{R}_{FSS\_i}^{180}\right)^2} = 0.00608019$		$\chi_{FSS}^{900} = \sqrt{\frac{1}{18-1}\sum_{i=1}^{18}\left(R_{FSS\_i}^{900} - \hat{R}_{FSS\_i}^{900}\right)^2} = 0.0006012$	
Limit of Detection (pM)		$LOD_{FSS}^{180} = 3\left\lvert\chi_{FSS}^{180}/S_{FSS}^{180}\right\rvert \approx 62.148$		$LOD_{FSS}^{900} = 3\left\lvert\chi_{FSS}^{900}/S_{FSS}^{900}\right\rvert \approx 0.9298$	

Table S2. Statistical results of Pb^{2+} detection results from SG-GFETs.

Pb^{2+} Conc. c (pM)	**Device number (i)**	**180-s observation**		**900-s observation**	
		Conductivity variation $R_{SG}^{180}(c) = \Delta\sigma_{SG}^{180}(c)$ (mS)	**Linear calibration value $\hat{R}_{SG}^{180}(c)$ (mS)**	**Conductivity variation $R_{SG}^{900}(c) = \Delta\sigma_{SG}^{900}(c)$ (mS)**	**Linear calibration value $\hat{R}_{SG}^{900}(c)$ (mS)**
0	SG-GFET#1	0.004094667	0.001203099	-0.000805333	0.001284471
5	SG-GFET#2	0.00417284	0.000976971	-0.00242716	-0.000413757
	SG-GFET#3	0.003865333		-0.001734667	
	SG-GFET#4	-0.003096296		0.000403704	
20	SG-GFET#5	0.000184932	0.000298585	-0.002115068	-0.005508441
	SG-GFET#6	0.00558046		-0.00381954	
	SG-GFET#7	-0.000032432		-0.003332432	
50	SG-GFET#8	0.001103261	-0.001058187	-0.019396739	-0.015697808
	SG-GFET#9	-0.001705814		-0.017205814	
	SG-GFET#10	-0.0055425		-0.0131425	
200	SG-GFET#11	-0.0075225	-0.007842045	-0.0291225	N/A
	SG-GFET#12	-0.011402703		-0.026302703	
	SG-GFET#13	-0.016022093		-0.036222093	
500	SG-GFET#14	-0.019298901	-0.02140976	-0.030198901	N/A
	SG-GFET#15	-0.018112987		-0.024512987	
	SG-GFET#16	-0.022165476		-0.031665476	
Standard deviation (mS)		$\chi_{SG}^{180} = \sqrt{\frac{1}{16-1}\sum_{i=1}^{16}\left(R_{SG\_i}^{180} - \hat{R}_{SG\_i}^{180}\right)^2} = 0.00358064$		$\chi_{SG}^{900} = \sqrt{\frac{1}{10-1}\sum_{i=1}^{10}\left(R_{SG\_i}^{900} - \hat{R}_{SG\_i}^{900}\right)^2} = 0.00241344$	
Limit of Detection (pM)		$\mathrm{LOD}_{SG}^{180} = 3\left\lvert\chi_{SG}^{180}/S_{SG}^{180}\right\rvert \approx 237.341$		$\mathrm{LOD}_{FSS}^{900} = 3\left\lvert\chi_{SG}^{900}/S_{SG}^{900}\right\rvert \approx 21.320$	

References

1. Huh, S.; Park, J.; Kim, Y. S.; Kim, K. S.; Hong, B. H.; Nam, J.-M. *ACS Nano* **2011,** 5, (12), 9799-9806.
2. Vervuurt, R. H.; Kessels, W. M.; Bol, A. A. *Adv. Mater. Interfaces* **2017,** 4, (18), 1700232.
3. Lee, B.; Park, S.-Y.; Kim, H.-C.; Cho, K.; Vogel, E. M.; Kim, M. J.; Wallace, R. M.; Kim, J. *Appl. Phys. Lett.* **2008,** 92, (20), 203102.
4. McDonnell, S.; Pirkle, A.; Kim, J.; Colombo, L.; Wallace, R. M. *J. Appl. Phys.* **2012,** 112, (10), 104110.
5. Wang, H.; Wu, Y.; Cong, C.; Shang, J.; Yu, T. *ACS Nano* **2010,** 4, (12), 7221-7228.
6. Levesque, P. L.; Sabri, S. S.; Aguirre, C. M.; Guillemette, J.; Siaj, M.; Desjardins, P.; Szkopek, T.; Martel, R. *Nano Lett.* **2011,** 11, (1), 132-137.